A Multiwavelength Study of the Symbiotic Mira HM Sge with SOFIA and HST

Steven R. Goldman[1,2] , Ravi Sankrit[1] , Edward Montiel[2] , Sean Garner[2] , Nathan Wolthuis[2] , and Nicole Karnath[2,3,4]

[1] Space Telescope Science Institute, 3700 San Martin Drive, Baltimore, MD 21218, USA; sgoldman@stsci.edu
[2] SOFIA-USRA, NASA Ames Research Center, MS 232-12, Moffett Field, CA 94035, USA
[3] Space Science Institute, 4765 Walnut Street, Suite B, Boulder, CO 80301, USA
[4] Center for Astrophysics Harvard & Smithsonian, Cambridge, MA 02138, USA

Abstract

We have targeted the dusty symbiotic Mira system HM Sge with four instruments from the IR to the UV. We have used these observations along with archival observations to study how the system has been evolving after its 1975 nova-like outburst. We have detected rovibrational water emission in a symbiotic system for the first time using new EXES high-spectral-resolution infrared spectroscopy. The features, detected in emission, have velocities consistent with the systemic velocity but do not show any clear evidence of high-velocity outflows. Mid-infrared photometry and grism spectroscopy show that the oxygen-rich asymptotic giant branch dust and dust output have shown little to no change over the past 39 years. In the optical/UV, we detect three main [N II] nebular features that were detected 22 years ago. Two of these features show a small amount of movement, corresponding to average outflows speeds of 38 and 78 km s^{-1} since they were previously observed; some previously detected [N II] features are no longer visible. New UV spectroscopy has shown that the nebular environment continues to steadily relax after the system's 1975 outburst. The data suggest, however, that the temperature of the hot component has increased from 200,000 K in 1989 to greater than 250,000 K now. Our new and archival observations suggest that the evolution of the system after its outburst is swift with little to no major changes after a period of a couple of years.

1. Introduction

Symbiotic systems are interacting binary systems composed of a cool giant and a hot companion (e.g., white dwarf, neutron star). These stars were initially classified as *spectroscopically peculiar* by Annie Jump Cannon, as they hosted a combination of spectral features found in both hot and cool stars (Merrill 1940). Since that time, over 350 symbiotic systems (Galactic and extragalactic) have been confirmed (Belczyński et al. 2000; Merc et al. 2019, and references therein).

Symbiotic systems provide a unique opportunity to simultaneously study a range of poorly understood astrophysical processes. The two stars' close proximity results in the transfer of material through accretion from the cool companion to the hot companion. This material can also build up on the hotter companion resulting in large nova-like outbursts or "slow" nova.

In some symbiotic systems the cooler companion is highly evolved, undergoing significant dust production and mass loss. In these cases the outflows, dust properties, and dust content can be greatly influenced by the hotter companion. These are referred to as dusty (D)-type symbiotic systems as opposed to the more common (~80%; Belczyński et al. 2000) stellar or S-type (Webster & Allen 1975). We can use identified symbiotic systems to study how these dustiest evolved giants known as thermally pulsing asymptotic giant branch (TP-AGB) stars are affected by an extreme environment.

Highly evolved AGB stars in their thermally pulsing phase typically have outflow velocities between 10 and 20 km s^{-1} (Engels & Bunzel 2015; Goldman et al. 2017; Olofsson et al. 2022).[5] Far faster winds have been detected in symbiotic systems, AGB stars transitioning into planetary nebulae, and the stages following the AGB (Solf 1983; Liimets et al. 2018; Guerrero et al. 2020; Sahai et al. 2022). Episodic mass loss or recurrent novae can lead to winds with multiple components with velocities ranging from a few km s^{-1} to thousands of km s^{-1} (Beliakina et al. 1978; Belyakina et al. 1979; Stauffer 1984; Tomov et al. 2007, 2017).

Multiwavelength studies are critical for a comprehensive understanding of D-type symbiotics and their environments. We describe here observations obtained under a joint Hubble Space Telescope (HST)/SOFIA Directors' Discretionary program targeting HM Sge. In this paper we will describe the unique symbiotic system HM Sge using new and archival multiwavelength data to better understand the system's local environment, kinematics, and dust. The paper is organized as follows: Section 2 outlines our new observations and archival data sets relevant to our discussion, Section 3 discusses our comparative analyses and new detections of IR water emission features, and Section 4 gives our concluding remarks.

1.1. HM Sge

HM Sagittae (Sge) is a nearby symbiotic system composed of a cool, highly evolved oxygen-rich (M-type) AGB star accreting material onto a white dwarf (WD). The system has a distance measured by Gaia Data Release 2 of 1027 pc (Gaia

---

[5] We will henceforth refer to the TP-AGB phase of evolution when discussing the properties of AGB stars.

Table 1
Properties of HM Sge

Parameter	Value	Reference
R.A.	295.°48783	(1)
Decl.	16.°74436	(1)
Kinematics		
Proper motion	$-0.443, -7.104$ mas yr^{-1}	(1)
Binary separation	40 au	(2)[a]
Binary axis orientation	130° E of N	(2)[b]
Binary axis rotation rate	?	
Orbital period	>90 yr	(3)
AGB star		
Pulsation period	534 days	(4)
Pulsation amplitude	$\Delta I \sim 1$ mag	(4)
Spectral type	M7	(5)
Luminosity	1500–2000 $L_\odot$	(6)
Gas mass loss rate	$4 \times 10^{-6} M_\odot$ yr^{-1}	(6)
White dwarf		
Temperature	$> 250,000$ K	(6)

Notes.
[a] Updated assuming the newer distance listed above.
[b] Assuming no rotation since the observations (1999).
References. (1) Gaia Collaboration et al. (2018), (2) Eyres et al. (2001), (3) Richards et al. (1999), (4) Goldman et al. (2022), (5) Mürset & Schmid (1999), (6) this work.

Collaboration et al. 2018). A number of works have also attempted to determine the system's orientation and kinematics based on UV, optical, and radio data (Table 1).

HM Sge is a symbiotic system with one of the most recent nova-like outbursts, occurring as recently as 1975 (Dokuchaeva 1976). The system brightened six magnitudes in the optical, but unlike classical novae, the outburst remained near its peak brightness far longer than the expected few days (Ciatti et al. 1979). The outburst is suspected to be the result of a hydrogen shell flash on the accretion envelope of the WD (Stauffer 1984).

Observations from the radio to X-ray have allowed us to study the environment around HM Sge as well as its individual hot and cool components (see review by Hinkle et al. 2013). HM Sge's cooler AGB star component has a pulsation period of 527 days (Munari & Whitelock 1989; Mürset & Schmid 1999), an M7 spectral type, and is heavily reddened in the near-IR ($J - K \sim 3$ mag). These are all indicative of dust production, high mass loss, and a late stage of AGB evolution; less is known about the WD companion. Nussbaumer & Vogel (1990) noted a change in the effective temperature of the WD from 40,000 K in 1976, just after the outburst, to 170,000 K in 1989. They also found that the WD kept a consistent luminosity of $10^4 L_\odot$ during this time.

1.1.1. System Orientation

The distance to HM Sge has been of great interest because the binary separation and speeds of outflows can be estimated based on angular displacements and the distance. While the dust and morphology of the system have hampered previous attempts to measure the distance, it has now been measured more accurately with Gaia with an estimated error of $\sim 10.6\%$.[6]

---

[6] The morphology and large dusty convective envelope may result in underpredictions of the parallactic error. This tends to be more of a problem for far more-luminous AGB stars that have uncertainties greater than 20% (Andriantsaralaza et al. 2022).

The binary orientation has also been a matter of debate. Solf (1984) used narrowband UV spatial–spectral mapping to determined that the fastest outflows (post-outburst) were to the east and west of the system, suggesting a north/south binary axis. This was then corroborated by Richards et al. (1999) with extended radio continuum features also to the east and west and a model placing the Mira north of the WD. Schmid et al. (2000) then observed the polarization of the Raman O VI line, which showed polarization at 33° east of north,[7] nearly parallel to the previously estimated binary axis, yet suggesting a binary axis perpendicular to it at 123°. A similar binary angle was determined by Eyres et al. (2001), who suggested that, based on the peak brightness in UV and optical HST filters, the binary axis is around 130° with the WD to the north at a separation of 40 mas (shown later in the right panel of Figure 4). Assuming the distance determined by Gaia, this yields an angular separation of 40 au. The binary axis shows a clear preference for a diagonal (NE or NW) orientation, something that has been seen in many observations of HM Sge. Evidence also suggests a value of the orbital period of at least 90 yr (Kenyon 1986; Richards et al. 1999). The geometry/morphology of the system is not well known, but evidence has suggested a torus-like structure seen either pole-on or edge-on (Sacuto et al. 2007).

1.1.2. Outflows

The winds measured around HM Sge have varied greatly since its outburst. A Wolf–Rayet-type wind was observed during the three years following the outburst with velocities up to 2000 km s^{-1} (Beliakina et al. 1978; Wallerstein 1978; Belyakina et al. 1979; Stauffer 1984). Kwok & Leahy (1984) used X-ray fluxes from observations in 1979 to infer wind speeds based on estimates of the plasma temperatures of at least 700 km s^{-1}. This was followed by a similar measurement and estimate for observations in 1992 that corresponded to wind speeds of greater than 500 km s^{-1} (Muerset et al. 1997).

In addition to the swiftly moving wind thought to be associated with the outburst are slower winds likely linked to current or previous mass loss. Cho & Kim (2010) detected water and SiO maser emission with peak velocities of -94.4 and -98.9 km s^{-1}, respectively. High-resolution spatial–spectral mapping in 1983 along directions corresponding to four slit angles was used to identify three different velocity components in [N II] around 6548 and 6583 Å (Solf 1984). Bipolar outflows of around 46 km s^{-1} were observed to the east and west, linked to two narrow nebular lobes separated by 1″.5. Slower outflows of around 9.5 km s^{-1} were also observed to the north and south, as well as a 2.6 km s^{-1} outflowing component around the central region. Additional imaging and spectroscopy of [N II] in 1996 show a range of velocities, with the most redshifted emission (~ 65 km s^{-1}) to the southwest and the most blue-shifted (~ -50 km s^{-1}) to the northeast of the central nebula (Corradi et al. 1999). Some of these measured velocity components are shown in Figure 1, and show a velocity profile consistent with a binary axis of around 120° and a complex rotating morphology.

Raman-scattered O VI lines (6825 Å) have also been detected in HM Sge (Schmid et al. 2000; Lee & Kang 2007). Lee & Kang (2007) found that these lines suggest a Keplerian disk around the WD star with an outer disk velocity of 26 km s^{-1}

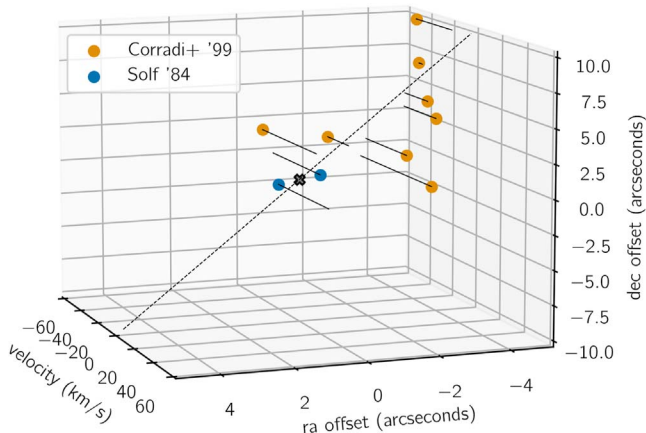[7] We will henceforth refer to all angles using this reference frame.

Figure 1. A subset of the velocities measured by previous observations of [N II] emission. Emission is blueshifted above the dashed line and redshifted below, suggesting potential rotation and a binary axis parallel or perpendicular to this axis of ∼120°.

and a terminal velocity of the AGB component of 10 km s^{-1}. In addition to plasma temperature and velocity-shifted emission, the proper motions of nebular features allow us to estimate average transverse velocities.

1.1.3. Nebular Features

Kwok et al. (1984) and Richards et al. (1999) used the Very Large Array (VLA) to measure the motion of nebular features in the radio continuum. Kwok et al. (1984) measured an average outflow of 0″024 yr^{-1} away from the system in the NNW direction, or around $v_{exp} \sim 56$ km s^{-1} ($\times D/1$ kpc). Richards et al. (1999) used four epochs over five years to measure a movement of two discrete nebular features attributed to rotation, with an average value of 2°5 ± 0°5 yr^{-1}. Richards et al. (1999) also detected features to the east and west that were brighter at low frequencies, suggesting that they may be nonthermal. They proposed that this may be synchrotron emission from the hot WD wind colliding with the dense blobs in the Mira wind.

HST/Faint Object Camera (FOC) optical images identified the presence of a slightly extended halo photoionized by the radiation from the hot component (Hack & Paresce 1993). HST/WFPC2 images obtained in 1999 showed nebular emission out to ∼2″ with the brightest knots within 0″5 of the central binary system (Eyres et al. 2001). Ground-based emission line images in the [N II], [O III], and Hα filters were obtained using the Nordic Optical Telescope (NOT). The [N II] images revealed the presence of a ∼30″ nebula, indicating an earlier episode of mass loss from the central system. Spectra obtained at the same time showed that the kinematics in the inner nebula was consistent with a rotating inner torus whereas the outer nebula displays a string of knots indicative of episodic mass ejection (Corradi et al. 1999). Several works have also studied the conditions within the nebular environment. We will discuss these further in Section 3.1.

1.1.4. Post-outburst Brightness

HM Sge dimmed by several magnitudes in the optical after its outburst in 1975. In near-IR photometry from the AAVSO, however, the system increased in brightness by an average of 0.092 mag yr^{-1} from 2010 to 2022 (Figure 2). The I-band light curve shows a fairly regular pulsation period. We fitted this

light curve using a Lomb–Scargle technique to determine a pulsation period of ∼540 days, similar to previous estimates (Goldman et al. 2022). The B-, V-, I-, and R-band photometry has also trended downward in the past several years. In the mid-1980s HM Sge also underwent a dimming in the infrared thought to be related to dust obscuration (Munari & Whitelock 1989). This dimming may be linked to a recent mass loss event resulting in increased dust obscuration, or may possibly be linked to the orbital motion of the system.

2. Observations

We have observed HM Sge using the HST and the Stratospheric Observatory for Infrared Astronomy (SOFIA; Temi et al. 2018). Here we compare our new observations with archival observations taken over the last 50 years. We compare new and old data from UV spectroscopy, near-UV + optical imaging, and IR photometry + spectroscopy, and present new high-resolution IR spectroscopy probing the outflow and accretion of water throughout the system.

2.1. COS

Observations using the Cosmic Origins Spectrograph (COS) on HST were obtained on 2021 March 21. Three positions were targeted—one centered on the stellar system and the others on nearby nebular features to the north and south. Spectra were obtained with the low-resolution grating modes G140L/800 in the far-UV (FUV) and G230L/2950 in the near-UV (NUV). We did not detect any emission in the offset positions, and therefore in this paper we will restrict our attention to only the emission from HM Sge and the 2″5 diameter region around it that is included in the COS aperture.

The effective wavelength coverage of the FUV spectrum is 912–1948 Å obtained on a single detector segment. The NUV spectrum contains three stripes, with stripe A covering 1720–2125 Å and stripe B covering 2811–3214 Å. Stripe C is contaminated by second-order light, and did not provide useful data. The FUV and NUV data have spectral resolutions $\lambda/\Delta\lambda$ of about 1100 and 500, respectively. For our analysis, we use the calibrated data available from MAST, downloaded on 2022 October 7. The data have been reprocessed using the updated reference files that have been normalized to the latest CALSPEC models and have an improved extraction for the NUV data (COS STScI Analysis Newsletter, 2022 March). All of the HST data used in this paper can be found in MAST: doi:10.17909/7gnq-a471.

2.2. WFC3/UVIS

Observations using HST's Wide-Field Camera 3 Ultraviolet–Visible channel (WFC3/UVIS) were taken on 2021 April 1. The observations included short exposures in three narrowband filters: F656N (Hα), F658N ([N II]), and F502N ([O III]). These exposures are used to image HM Sge's inner nebula. An additional, longer exposure was taken in the F658N filter with the goal of reaching a similar sensitivity to the previous NOT observations. We use the calibrated data available from MAST, downloaded on 2021 June 9. These are used to study the morphology of the more extended surrounding nebula while saturating on the central source. We will compare these observations to archival observations from the NOT (Corradi et al. 1999) and HST/WFPC2 (Eyres et al. 2001) to study
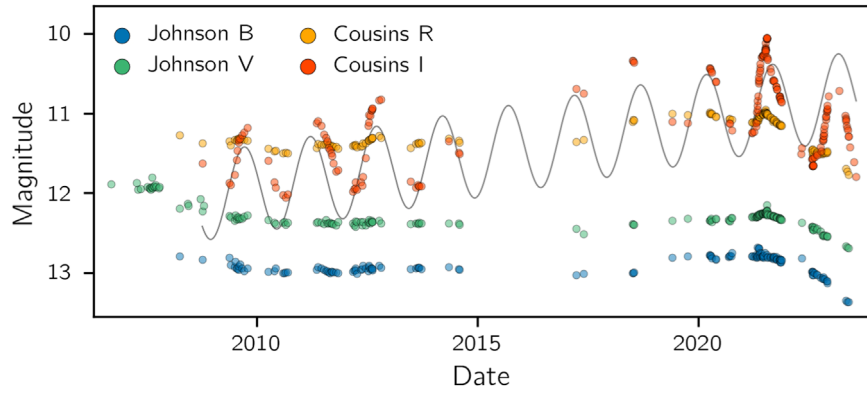
Figure 2. The brightness of HM Sge in *BVIR* filters from a subset of the available AAVSO data. We fit a sinusoidal function to the *I*-band data, showing a general increase in the IR flux independent of variability; the system, however, has dropped in brightness in the *I b*and. Adapted from Goldman et al. (2022).

changes in the nebular structure and measure proper motions of nebular features.

2.3. FORCAST

Observations were taken using the Faint Object Infrared Camera (FORCAST; Herter et al. 2018) on board SOFIA on the nights of 2021 July 1 and July 8. The observations include imaging in all ten available photometric filters, as well as grism spectroscopy with the FOR_G111 (8.4–13.7 μm) and FOR_G227 (17.6–27.7 μm) gratings.

Photometry. The imaging observations use standard chopping-and-nodding techniques to remove image artifacts and spurious detections. We perform aperture photometry for each of our filters using the standard reduction. Relative photometric statistical uncertainties were estimated using an annulus background (typically $\sim$5%). Photometric filters with their exposure times and effective wavelengths are listed in Table 2 of the Appendix. The point-spread function estimated for the data is $\sim$3″5, and we find that the IR emission lies spatially within a similar radius.

Grism spectroscopy. Grism spectra were obtained in the FOR_G111 and FOR_G227 settings using the 4″7 wide slit, yielding spectral resolutions of $R = 110$ and $R = 130$, respectively. We use the standard calibrated Level 3 data provided by the SOFIA Science Center. Systematic errors for FORCAST grism spectroscopy can be as large as 10% due to atmospheric conditions and slit misalignment. To get a more accurate absolute flux scaling we have normalized our spectra using the contemporaneous FORCAST photometry. We use the flux averages of the spectra, weighted by the filter transmission, and shift the spectra to the level of the FOR_F111 and FOR_F253 flux for the G111 and G227 spectra, respectively. This corresponds to shifts of 3.35 and -7.06 Jy for the G111 and G227 grisms, respectively. Our data are severely affected by atmospheric ozone between 9.2 and 10.3 μm, and we exclude these data from our analysis.

2.4. EXES

Observations using the Echelon-Cross-Echelle Spectrograph (EXES; Richter et al. 2018) instrument on board SOFIA were taken on 2021 December 4, 2022 March 1, 2022 March 5, and 2022 April 27 with three unique and two duplicated settings. The angular resolution of the observations ranged from 1″8 to 2″3. All observations were taken with a channel width of $\sim$5 nm and spanned a spectral range from 5.70 to 7.62 μm with

Table 2
FORCAST Imaging Observations of HM Sge

Date	Filter	$\lambda_{\mathrm{effective}}$ (μm)	$T_{\mathrm{exp.}}$ (s)
2021 Jun 1	FOR_F056	5.60	29
2021 Jun 8	FOR_F064	6.35	146
2021 Jun 8	FOR_F077	7.69	66
2021 Jun 1	FOR_F111	11.06	111
2021 Jun 8	FOR_F197	19.36	41
2021 Jun 8	FOR_F253	25.33	140
2021 Jun 8	FOR_F315	31.10	50
2021 Jun 8	FOR_F336	33.52	219
2021 Jun 8	FOR_F348	34.58	159
2021 Jun 1	FOR_F371	36.99	100

a resolution of $R = 60,000$ ($v = 5.0$ km s^{-1}). The slit width was $\sim$3″2 and the slit length was between 8″85 and 9″6. We identify a number of rovibrational water emission features that probe the dusty outflows of the cooler component of HM Sge. We will use these to better understand the kinematics of the material surrounding HM Sge.

2.5. Archival Observations

Here we list the main observations used for our comparative analyses. For a more complete list of the archival observations of HM Sge see Table 5 of the Appendix.

NOT. The NOT was used for imaging in several narrowband filters (Hα, [N II], [O I], [O II], [O III]), as well as spectroscopy around the [N II] 6583 Å line at three positions and angles (Corradi et al. 1999). The data were not available online, but were provided by the authors (Romano Corradi, private communication). The data show clear detections of nebular features in the [N II] filter with similar fainter structures in the [O II] filter. The spectra were used to measure radial velocities for the nebular features with velocities between -50 and 65 km s^{-1}. Position-matching on bright sources was used to align the NOT images with our new WFC3 images.

ISO. The Infrared Space Observatory (ISO) was used to observe HM Sge in 1996 and 1997 (Schild et al. 2001) with the Short Wavelength Spectrometer (SWS) and Long Wavelength Spectrometer (LWS), and the data show clear detections of the 10 and 18 μm silicate features in the SWS data. We downloaded the SWS spectra from the ISO data archive; the
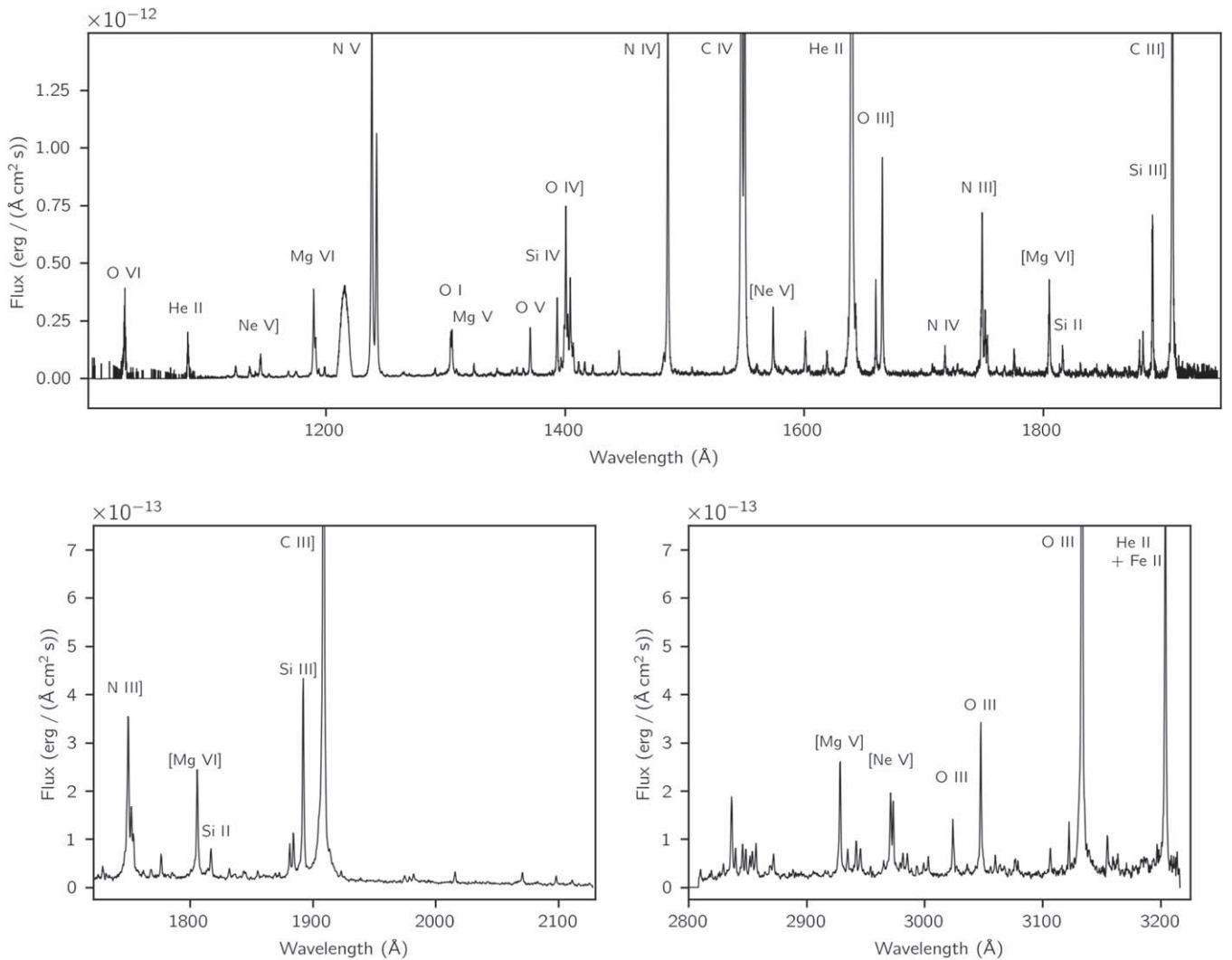
Figure 3. HST/COS NUV and FUV spectra showing the UV emission lines in the nebular environment around HM Sge.

longer-wavelength (43–196 μm) LWS data and Spitzer MIPS data also exist, but are not discussed in this work as we have not obtained new longer-wavelength data for comparison. A number of nebular lines are detected in these spectra, including some from highly ionized species such as [Ne V] and [Ne VI]. The strongest line detected is [Ne VI] $^2P_{3/2}$–$^2P_{1/2}$ at 7.6524 μm, which was also observed with VLTI/MIDI (Sacuto et al. 2007).

IUE. The International Ultraviolet Explorer (IUE) was used to observe HM Sge many times between 1978 and 1992. The early data, analyzed by Mueller & Nussbaumer (1985), show that between 1979 June and September there was a dramatic increase in the brightness of the high-ionization lines He II 1640 Å, C IV 1550 Å, and N V 1240 Å. The brightness of these lines increased rapidly up to 1985, and then remained at about the same level until 1989, while in the latter period, lower-ionization lines such as the semiforbidden N III] 1750 Å and O III] 1664 Å lines (denoted with a single bracket) started declining in brightness (Nussbaumer & Vogel 1990). The model proposed by Nussbaumer & Vogel (1990) to explain the evolution of the UV emission line spectrum was photoioniza-tion of nebular material by the radiation from the hot star (and possibly an accretion disk) that was increasing in temperature

while emitting at constant luminosity. Formiggini et al. (1995) presented a model for HM Sge that included both photoioniza-tion and a shock due to colliding winds expected in symbiotic systems (Girard & Willson 1987). Their conclusions about the nature of the photoionization source agree with Nussbaumer & Vogel (1990). Additionally they find that the lower-ionization line strengths are better explained if shock excitation is included, with the shock velocity decreasing from about 300 km s^{-1} to 180 km s^{-1} between 1979 and 1990. Murset & Nussbaumer (1994) used the IUE data to estimate the temperature of the ionizing source at different epochs. They noted the presence of [Mg VI] lines in 1990 October, which were not there in 1989 November, and inferred that the radiation temperature had increased from 170,000 to 200,000 K.

3. Results and Discussion

We will start by discussing the results that focus broadly on the environment surrounding the system, we will then move inward to discuss the kinematics of the material moving within and away from the system, and then discuss the properties of the stellar components of the system, particularly the dust surrounding the AGB star.

Table 3
UV Emission Lines in the COS Spectra of HM Sge

Ion	Wavelength (Å)	Flux[a]	Change from 1989[b]
FUV G140L/800			
O VI	1032	5.4	…
He II	1085	2.3	…
Ne V]	1136	0.7	…
Ne V]	1145	1.6	…
Mg VI	1189, 1191	7.0	…
N V	1238, 1242	45.2	+10%
O V	1371	2.3	=
O IV] + Si IV	1400	27.0	=
N IV]	1485	27.3	−20%
C IV	1548, 1551	111.0	−30%
[Ne V]	1575	3.6	−28%
[Ne IV]	1601	2.2	−78%
He II	1640	122.0	+36%
O III]	1660	4.0	=
O III]	1666	11.1	=
N IV	1719	1.2	=
N III]	1750	15.3	−24%
Mg VI	1806	5.4	new[c]
Si II	1816	1.3	−35%
Si III]	1892	8.3	=
C III]	1909	42.0	−35%
NUV G230L/2950			
[Mg V]	2929	4.7	−53%
[Ne V] + Fe II	2973	4.6	−23%
O III	3023	2.0	−50%
O III	3047	4.7	−48%
O III	3133	39.0	−34%
He II + Fe II	3204	14.6	−36%

Notes.
[a] Units of 10^{-13} erg s^{-1} cm^{-2}.
[b] Change since 1989 November, from Table 2 of Nussbaumer & Vogel (1990).
[c] This line was not detected in the 1989 IUE spectrum.

3.1. Ultraviolet Emission

The calibrated COS spectra are shown in Figure 3. The top panel shows the G140L/800 FUV data, and the bottom panels show stripes A and B of the G230L/2950 NUV data. A large number of lines are detected and their fluxes span a wide range. Most of the strong and medium-strength lines are labeled in the figure. A number of the weak lines are from either Fe II or Fe III, or else are unidentified. In this paper, we do not consider any of these weaker lines, nor any of the medium-strength Fe lines, of which there are a few. Rather, we focus on lines detected in IUE spectra, and analyzed by Mueller & Nussbaumer (1985) and Nussbaumer & Vogel (1990)

The measured fluxes of a selected set of lines are given in Table 3. The last column tabulates the change in the observed line strengths between the COS spectra and the most recent IUE spectra presented in Nussbaumer & Vogel (1990). In many cases, although doublet and multiplet lines are resolved in our spectra we tabulate the total flux for ease of comparison with the earlier measurements and discuss individual component strengths where relevant. For the region of overlap, we report measurements obtained using the FUV spectrum. The NUV Stripe A spectrum was used to check for consistency.

The most obvious change between the 1989 and 2021 spectra is the significant decrease in most of the line strengths, ranging from −20% for the semiforbidden N IV] λ1485 to −78% for the forbidden [Ne IV] λ1601 line. A few line strengths have stayed about the same, and two have increased: N V λλ1238, 1242 by 10% and He II λ1640 by 36%. Another notable difference is that Mg VI λ1806, which was not detected in 1989, is fairly strong in the COS spectrum. Additionally, several lines are detected at wavelengths shortward of 1200 Å, which were not covered by IUE. Of these, O VI λ1032 and He II λ1085 lie in a region of low throughput and are only weakly detected.

A detailed study of the evolution of the UV spectra since 1989 is ongoing and will be the subject of a future publication. Here we limit ourselves to a general interpretation of the changes observed. The increase in the strength of the high-ionization lines is evidence that the ionizing source has continued to become hotter. The [Ne V] λ1575/[Ne IV] λ1601 flux ratio suggests that the effective temperature now is at least 250,000 K (Table 5 of Nussbaumer & Vogel 1990), whereas it was less than 200,000 K in 1989.

There are probably multiple reasons for the decrease observed in many emission line fluxes. Some of it may be due to the gas being ionized to higher states. This would explain, for instance, the decrease in both [Ne V] and [Ne IV] as a larger fraction of the gas would be ionized up to Ne IV. The separation between the two components may have increased due to orbital motion, which would imply a weaker photoionizing flux at the nebular interface and a decrease in line strengths. The COS data are not sufficient to discriminate between these scenarios or to address the possibility of changes in elemental abundances leading to changes in line strengths.

Formiggini et al. (1995) found that the wind collision shock had grown weaker with time since the explosion, but still contributed significantly to the low-ionization lines observed in the 1987–1988 IUE spectra. Specifically their models showed a decrease in the shock velocity from around 300 km s^{-1} in 1979 to 180 km s^{-1} a decade later. The continued presence of a shock, with even a still lower velocity, would be a possible reason why some of the lines have not decreased in strength, because they would be collisionally excited rather than photoionized. This would help explain why the O III] λλ1660, 1666 line strengths have remained constant while the O III Bowen fluorescence lines have become significantly fainter.

3.2. Tracing Ionized Ejecta with [N II]

Our new HST WFC3 [N II] imaging data of HM Sge show a variety of structures at differing levels of brightness (Figure 4). When we compare 1996 NOT observations to the 2021 WFC3 HST observations, we can identify several prominent common nebular features to the northwest of the system (Figures 5 and 6); we will refer to these as features A, B, and C. These features show a small amount of movement between 1996 and 2021. Several additional smaller and faint common features are visible to the southeast and southwest.

We have used a magnification technique similar to that of Reed et al. (1999) and Palen et al. (2002) to estimate the average outflow speed of features A and B. By taking a region of the WFC3 data, iteratively decreasing the pixel scale (demagnifying), degrading it to the resolution of the NOT, subtracting the image, and calculating the standard deviation,
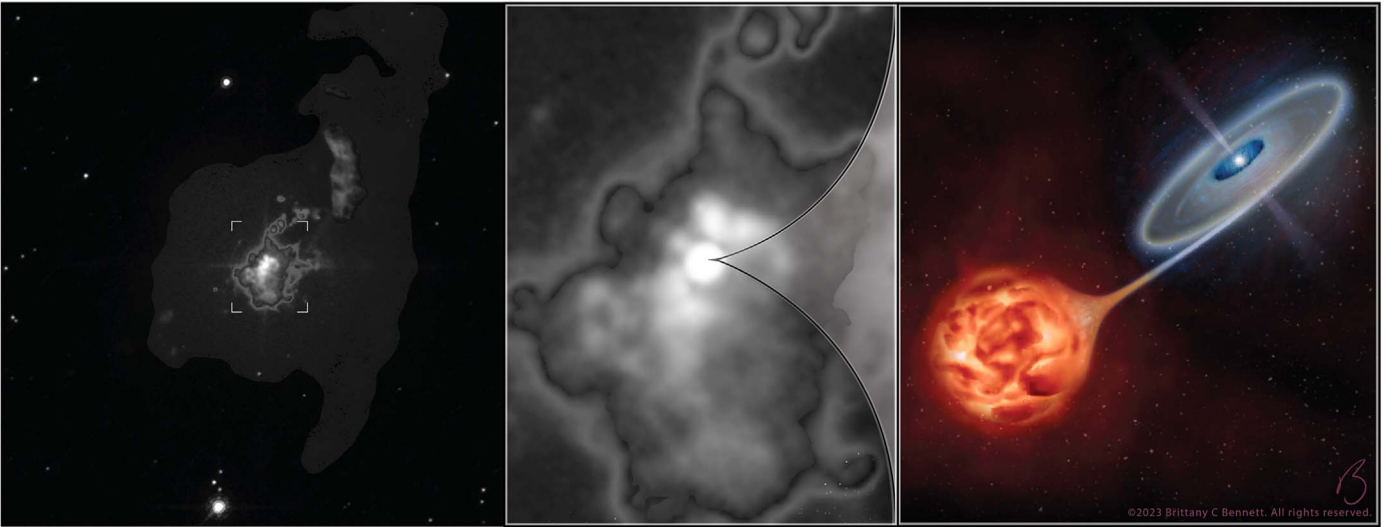
Figure 4. HST WFC3 [N II] image of HM Sge and the surrounding nebula enhanced artistically to accentuate the main nebular features of different contrast scales for the large-scale nebular structure (left) and central region (center). Also shown is an illustration of the inner stellar components of HM Sge (right), showing the suspected orientation and location of the hot and cold components; there are uncertainties in the orientation, which are discussed further in Section 3.2. © 2023 Brittany C. Bennett. All rights reserved. Used with permission.
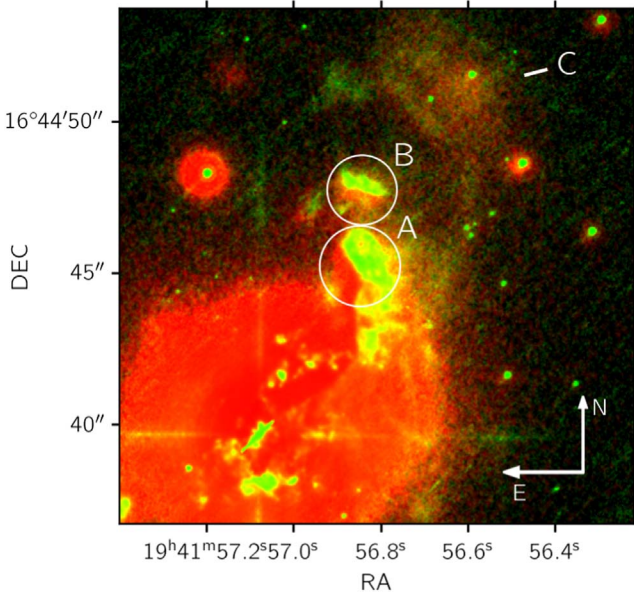

Figure 5. A red (NOT)/green (HST/WFC3) image of the northwest region of HM Sge in narrowband [N II] optical filters. The image shows the evolution of three main nebular features (that we identify as A, B, and C) over a period of 22 years. The vertical/horizontal crosshair pattern around the central source (lower left) is the result of saturation.

we are able to determine the best-fitted spatial shift of features A and B (Figure 7). This technique allows for an estimate of the shift with precision below that of the NOT pixel scale. Using this technique we find best-fitted spatial shifts of $0.''40$ and $0.''19$ for features A and B, respectively. Using the time difference between the observations yields average outflow speeds for features A and B of $78 \, \mathrm{km \, s^{-1}}$ and $38 \, \mathrm{km \, s^{-1}}$, respectively.

Given the distance to the system and the angular distance from the central region to the most prominent common features (A: $6.''3$, B: $8.''7$, C: $13''$), these would have to have been

moving at average velocities of 1500, 2000, and $3000 \, \mathrm{km \, s^{-1}}$ respectively, since the outburst to be at the distances observed in 1996. Outflows at these speeds have not been detected since the outburst, suggesting they are from the 1975 outburst or, more likely, previous outbursts. The outflow speed of feature A, and the lower outflow speed for feature B farther out, are likely the result of shocks. Fast winds from previous outbursts have likely interacted with the material at large radii, slowed down and thermalized, and contributed to the slow outward movement and evolution of the nebula.

Data have shown evidence of $\sim 100 \, \mathrm{km \, s^{-1}}$ outflows possibly linked to jets. Outflows with these speeds have been detected in the radio (Cho & Kim 2010) and optical (Corradi et al. 1999), and inferred in the X-ray (Toalá et al. 2023). We do not detect any jet-like outflows blowing out material at high speeds. While this does not discount the existence of jets, if they do exist, we do not see any evidence of them where we detect nebular emission. Higher-speed outflows may also be blowing out material in regions void of nebular material. Any small movement in the nebular features that we see may be attributed to the difference in resolution, ionization of the inner nebula, or slower movement of these features. We also have data in the Hα and [O III] filters. The Hα data are primarily saturated with one common feature north of the central nebula. The [O III] data also show several common features but no extended emission outside $3.''5$.

By comparing our F502N [O III] data with the 1999 WFPC2 observations we get a better view of the central region. We see a similar morphology to that seen in 1999 but seemingly rotated in the clockwise direction. This may suggest a rotation opposite to what was determined by Richards et al. (1999), but may also reflect different parts of the nebula changing in brightness in [O III]. We also see additional extended emission that may be new or below the WFPC2 detection threshold. To better understand the outflows of the system, we have also targeted the rovibrational lines of water in the IR to measure the movement of material closer to the stars.
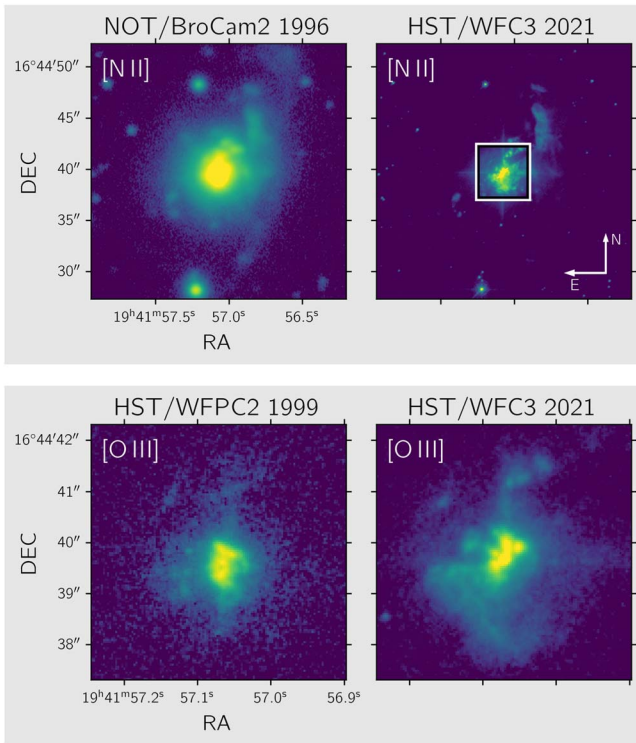
Figure 6. A comparison of new and archival narrowband optical images of HM Sge. The white box is the zoomed-in region shown in the lower images; intensities are displayed on a logarithmic scale.
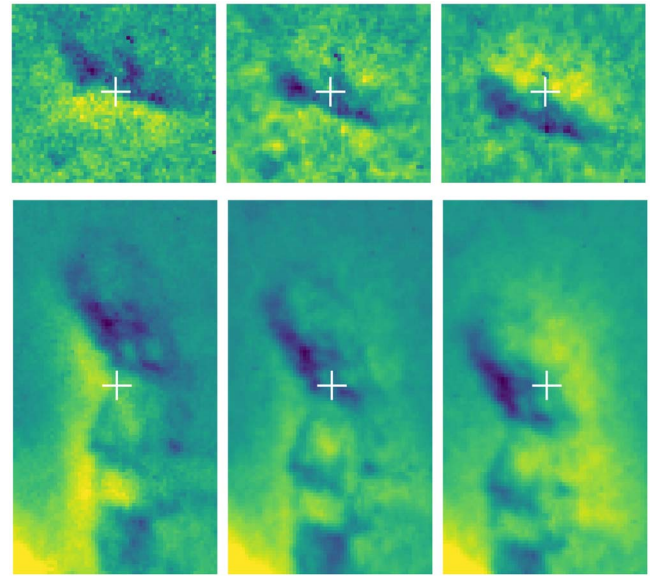

Figure 7. The (de)magnification technique used to fit the spatial shift of features A (bottom) and B (top) between the WFPC2 (1996) and WFC3 (2021) [N II] images. The initial normalized image differences (left) are shown along with the best-fitted shift image (center) as well as a further demagnified source (right). Darker features are from WFC3 data that move down and to the left as we decrease the WFC3 pixel scale.

3.3. Wind Velocities from H₂O Emission

HM Sge was targeted with EXES to detect velocity-shifted rovibrational water lines that allow us to probe the kinematics of the winds surrounding the AGB and accretion disk. The four observations in three unique settings are displayed in Figure 8. In the figure we also show ATRAN telluric model spectra, as well as molecular transitions of water from HITRAN. We find that most of the emission features have small offsets ($<10 \, \text{km s}^{-1}$) from our assumed systemic velocity[8] of $-5 \, \text{km s}^{-1}$ (Hinkle et al. 2013), giving more evidence for this as the systemic velocity. We also detect three lines with velocity shifts of $\sim30 \, \text{km s}^{-1}$; all of these lines are listed in Table 4.

The small velocity shifts that we see in emission may be probing the material moving away from the cool component. In spherically symmetric AGB stars, we expect a slow dense wind expanding radially outward as the star loses mass and produces dust. This wind may be even slower along the line of sight for a source like HM Sge, which likely has higher-velocity bipolar outflows in the NW or NE direction. Assuming spherical symmetry and lines that are optically thick, these features should peak at the systemic velocity (Wannier et al. 1990). EXES data of other molecular features in nearby AGB stars (e.g., Fonfría et al. 2008) have shown emission features at or near the systemic velocity, and we see this in most of our water emission lines. The emission features have narrow peak widths representative of outflows with little to no outward velocity.

In addition to the emission features seen near the systemic velocity, we detect three emission lines that do appear to be associated with multiple peaks. Lee & Kang (2007) fit models

of the Raman O VI λ6825 line and determined an outflow velocity of the AGB star around $10 \, \text{km s}^{-1}$ and that the WD hosts a Keplerian disk with an outer rim velocity of $26 \, \text{km s}^{-1}$. We detect three emission lines around 5.710–5.725 μm that have a velocity-shifted peak at a few km s^{-1} and $\sim30 \, \text{km s}^{-1}$. Given the similarity in the predicted and observed velocities, we may be probing the Keplerian disk around the WD. Accretion has been measured in absorption in similar rovibrational water lines in young stellar objects (Indriolo et al. 2020) but not before in emission; infrared water absorption bands in the 1–5 μm range were also noted by Bregman (1982). While we do not detect any clear water features in absorption, the disk may not be optically thick because the dust and IR emission appear to be concentrated on the AGB star. We also see one tentative detection of an emission line velocity shifted by $-76.7 \, \text{km s}^{-1}$, which may be probing the jets of the system.

Several water emission features were detected in both 2021 December and 2022 April in our 6.7 μm setting. These lines are non-Gaussian in both epochs and tend to have a systemic peak velocity shift of around $2 \, \text{km s}^{-1}$, except for the line at 6.75107 μm, which has a $10 \, \text{km s}^{-1}$ shift between observations. Given our velocity resolution of $0.3 \, \text{km s}^{-1}$ in this setting, we expect the shift is real. We expect that the bulk of the water emission is coming from close-in to the system, $\lesssim70$ au (Gray et al. 2022) or 0.″01 at the distance of HM Sge. These are far smaller scales than those resolvable by EXES (1.″8–2.″3). The two settings have position angles that are nearly orthogonal, with the December setting at $\sim327°$ (oriented in the northwest direction) and the March section at $\sim230°$ (Figure 9). Given the suspected location of the emission, the difference in position angle is unlikely to be the cause of the small systemic velocity shift. Further analysis of these data will be conducted in future works.
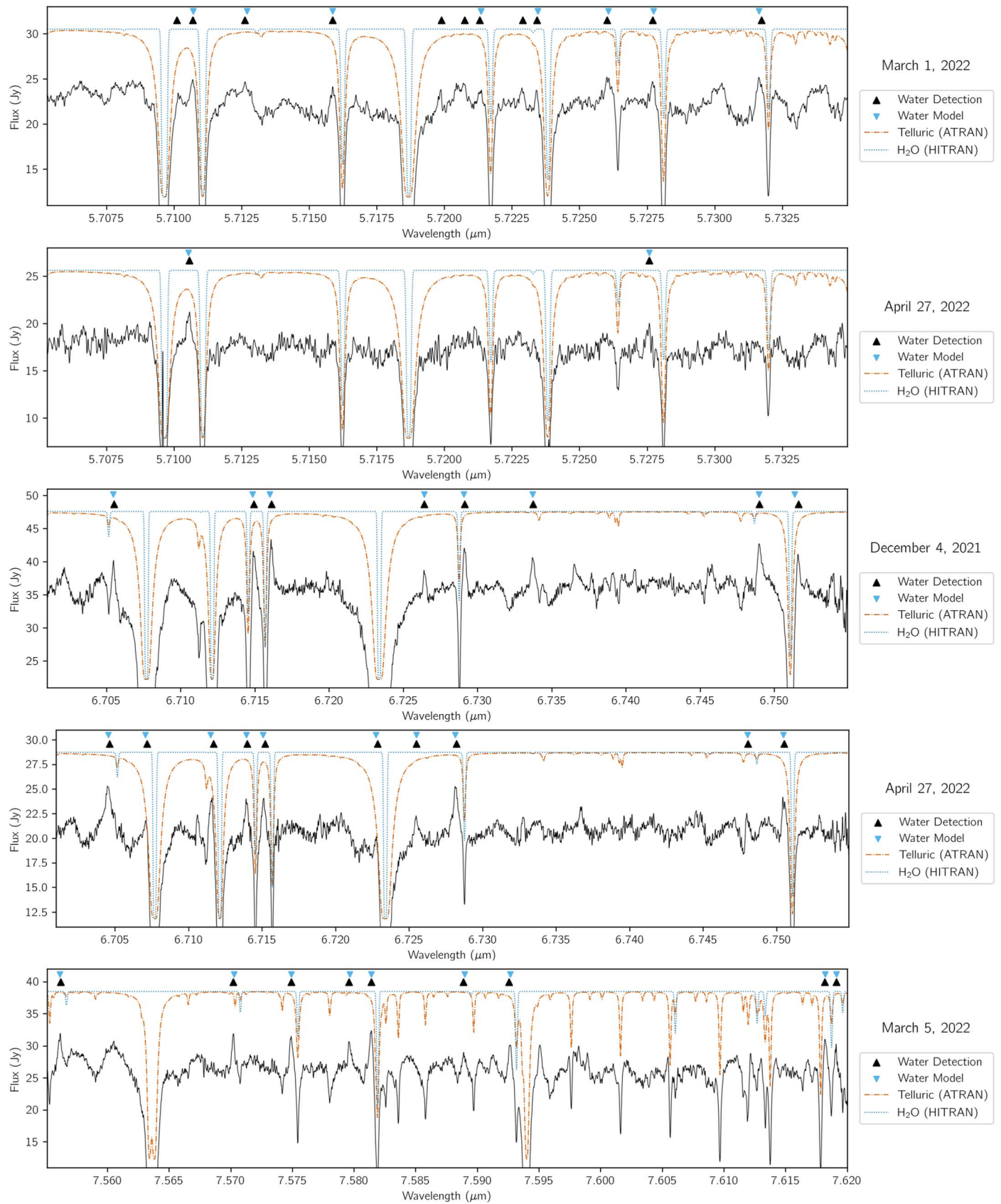
---

[8] The spectra are corrected for the velocity shifts from the seasonal motion of the Earth.

Figure 8. Infrared water emission features detected in high-resolution EXES spectra (black), which probe the kinematics of material around HM Sge. We show the ATRAN telluric model spectra (red) and HITRAN model spectra of water (blue). The features are velocity-shifted by the seasonal motion of the Earth, and the observations were scheduled so that these features fall in the wings of telluric features. The wavelengths of suspected water emission features and their corresponding model features at the system velocity are shown with black and blue triangles above the features.

Table 4
Results of EXES Observations

Date	$v' - v''$	$J_{Ka,Kc}' - J_{Ka,Kc}''$	$\lambda_{\text{Observed}}$ (μm)	λ_{Model} (μm)	Velocity Shift[a] (km s^{-1})	Upper State Energy (K)	Einstein Coefficient (s^{-1})
2022 Mar 1	$v_2 = 1 - 0$	$8_{0,8} - 7_{1,7}$	5.71009	5.71107	−31.9	3363.1	12.4
2022 Mar 1	$v_2 = 1 - 0$	$8_{0,8} - 7_{1,7}$	5.71069	5.71107	−0.5	3363.1	12.4
2022 Apr 27	$v_2 = 1 - 0$	$8_{0,8} - 7_{1,7}$	5.71056	5.71107	1.9	3363.1	12.4
2022 Mar 1	$v_2 = 1 - 0$	$11_{3,8} - 11_{2,9}$	5.71261	5.71306	−4.3	4950.9	3.2
2022 Mar 1	$v_2 = 1 - 0$	$6_{4,3} - 6_{3,4}$	5.71586	5.71623	−0.3	3450.8	2.9
2022 Mar 1	$v_2 = 1 - 0$	$5_{4,2} - 5_{3,3}$	5.71988	5.72171	−76.7	3239.7	2.4
2022 Mar 1	$v_2 = 1 - 0$	$5_{4,2} - 5_{3,3}$	5.72074	5.72171	−31.5	3239.7	2.4
2022 Mar 1	$v_2 = 1 - 0$	$5_{4,2} - 5_{3,3}$	5.72131	5.72171	−1.9	3239.7	2.4
2022 Mar 1	$v_2 = 1 - 0$	$4_{4,1} - 4_{3,2}$	5.72342	5.72383	−2.0	3064.0	1.6
2022 Mar 1	$v_2 = 1 - 0$	$4_{4,1} - 4_{3,2}$	5.72289	5.72383	−29.8	3064.0	1.6
2022 Mar 1	$v_2 = 1 - 0$	$8_{1,7} - 8_{0,8}$	5.72601	5.72643	−2.3	3583.1	1.4
2022 Mar 1	$v_2 = 1 - 0$	$4_{4,0} - 4_{3,1}$	5.72770	5.72811	−1.9	3064.1	1.6
2022 Apr 27	$v_2 = 1 - 0$	$4_{4,0} - 4_{3,1}$	5.72758	5.72811	0.5	3064.1	1.6
2022 Mar 1	$v_2 = 1 - 0$	$8_{3,6} - 8_{2,7}$	5.73173	5.73199	5.4	3784.3	2.7
2022 Apr 27	$v_2 = 1 - 0$	$10_{3,8} - 10_{4,7}$	6.70462	6.70516	4.2	4421.0	9.6
2021 Dec 4	$v_2 = 1 - 0$	$10_{3,8} - 10_{4,7}$	6.70549	6.70516	1.9	4421.0	9.6
2022 Apr 27	$v_2 = 1 - 0$	$4_{0,4} - 5_{1,5}$	6.70715	6.70770	4.1	2614.9	8.6
2022 Apr 27	$v_2 = 1 - 0$	$6_{1,6} - 6_{2,5}$	6.71168	6.71212	8.3	2939.1	4.9
2022 Apr 27	$v_2 = 1 - 0$	$6_{3,4} - 7_{2,5}$	6.71399	6.71455	3.2	3268.5	1.9
2021 Dec 4	$v_2 = 1 - 0$	$6_{3,4} - 7_{2,5}$	6.71491	6.71455	3.0	3268.5	1.9
2022 Apr 27	$v_2 = 1 - 0$	$8_{2,7} - 8_{3,6}$	6.71519	6.71569	6.1	3590.0	7.7
2021 Dec 4	$v_2 = 1 - 0$	$8_{2,7} - 8_{3,6}$	6.71611	6.71569	5.6	3590.0	7.7
2022 Apr 27	$v_2 = 1 - 0$	$2_{1,1} - 3_{2,2}$	6.72284	6.72337	4.3	2436.8	8.4
2022 Apr 27	$v_2 = 2 - 1$	$7_{1,6} - 7_{2,5}$	6.72548	6.72611	0.2	5581.6	20.3
2021 Dec 4	$v_2 = 2 - 1$	$7_{1,6} - 7_{2,5}$	6.72641	6.72611	0.1	5581.6	20.3
2022 Apr 27	$v_2 = 1 - 0$	$9_{1,8} - 9_{2,7}$	6.72820	6.72876	3.2	3867.6	7.9
2021 Dec 4	$v_2 = 1 - 0$	$9_{1,8} - 9_{2,7}$	6.72913	6.72876	3.2	3867.6	7.9
2021 Dec 4	$v_2 = 2 - 1$	$3_{2,1} - 3_{3,0}$	6.73372	6.73340	1.3	4881.5	9.1
2022 Apr 27	$v_2 = 1 - 0$	$8_{4,5} - 9_{3,6}$	6.74803	6.74865	1.0	3977.8	1.2
2021 Dec 4	$v_2 = 1 - 0$	$8_{4,5} - 9_{3,6}$	6.74898	6.74865	1.4	3977.8	1.2
2022 Apr 27	$v_2 = 1 - 0$	$5_{2,4} - 6_{1,5}$	6.75049	6.75107	2.6	2912.3	4.5
2021 Dec 4	$v_2 = 1 - 0$	$5_{2,4} - 6_{1,5}$	6.75161	6.75107	10.8	2912.3	4.5
2022 Mar 5	$v_2 = 1 - 0$	$9_{3,6} - 10_{4,7}$	7.55620	7.55667	2.0	4179.2	3.9
2022 Mar 5	$v_2 = 1 - 0$	$7_{7,1} - 8_{8,0}$	7.57018	7.57078	−3.0	4474.5	15.6
2022 Mar 5	$v_2 = 1 - 0$	$5_{1,5} - 6_{2,4}$	7.57490	7.57543	−0.6	2766.5	0.7
2022 Mar 5	$v_2 = 1 - 0$	$10_{3,7} - 11_{4,8}$	7.57958	7.58018	−3.2	4549.8	3.7
2022 Mar 5	$v_2 = 1 - 0$	$6_{2,5} - 7_{3,4}$	7.58140	7.58190	0.9	3109.6	2.2
2022 Mar 5	$v_2 = 1 - 0$	$13_{0,13} - 14_{1,14}$	7.58886	7.58949	−4.3	4879.1	5.7
2022 Mar 5	$v_2 = 1 - 0$	$7_{4,3} - 8_{5,4}$	7.59257	7.59318	−3.7	3700.8	7.5
2022 Mar 5	$v_2 = 1 - 0$	$7_{5,2} - 8_{6,3}$	7.61816	7.61872	−1.4	3919.5	10.1
2022 Mar 5	$v_2 = 1 - 0$	$7_{5,3} - 8_{6,2}$	7.61910	7.61963	−0.0	3919.3	10.1

Notes. Upper state energy is calculated by adding the lower state energy from the HITRAN database to the wavenumber of the feature. The Einstein coefficient is from the listed HITRAN water transition. Curly brackets indicate the same transition.
[a] Velocity shifts are corrected for the motion of Earth and the systemic velocity (5 km s^{-1}; Hinkle et al. 2013). While additional features may be visible, we focus on those most likely to be rovibrational water transitions.

3.4. Infrared Observations

The cool component of HM Sge is a thermally pulsing oxygen-rich AGB star, expected to be producing silicate-rich dust. This dust produces a characteristic 10 μm silicate feature in the IR that is highly sensitive to changes in dust properties and optical depth. This feature has been seen in HM Sge in several observations, giving us an idea of how the system's dust is evolving.

HM Sge was previously observed in the IR with IRAS, ISO, and VLTI/MIDI. The VLTI observations by Sacuto et al. (2007) showed that mid-IR emission is limited to small spatial scales (half-width at half-maximum ∼ 7.2 mas at 8.5 μm). They also found that the local intensity of the envelope at 20 mas is

less than 3% of the intensity at 4 mas, indicating minimal dust near the WD located at 40 mas. Unlike the previous observations in the IR, our FORCAST observations are affected by atmospheric ozone between 9.2 and 10.3 μm, shown in gray in Figure 10. The new and archival observations show the 10 μm silicate feature in emission with varying levels of continuum brightness. The continuum brightness has been steadily decreasing since the initial IRAS observations. Changes in the silicate feature in the FORCAST data are less pronounced but show some subtle differences. In particular, the shape of the full IR continuum has changed, growing brighter in the near-IR and fainter in the far-IR.

These stars can swiftly lose a considerable amount of their circumstellar envelope through dense outflows (up to
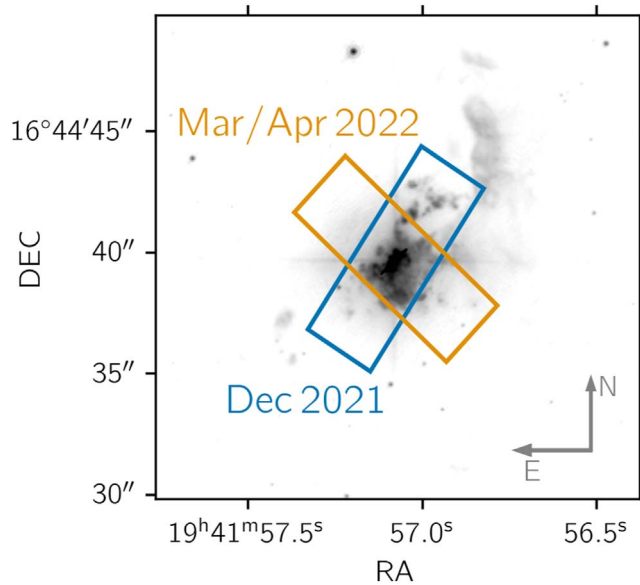
Figure 9. The EXES slit position for the two epochs of observation using the 6.7 μm setting overlaid on our new long-exposure HST [N II] image.
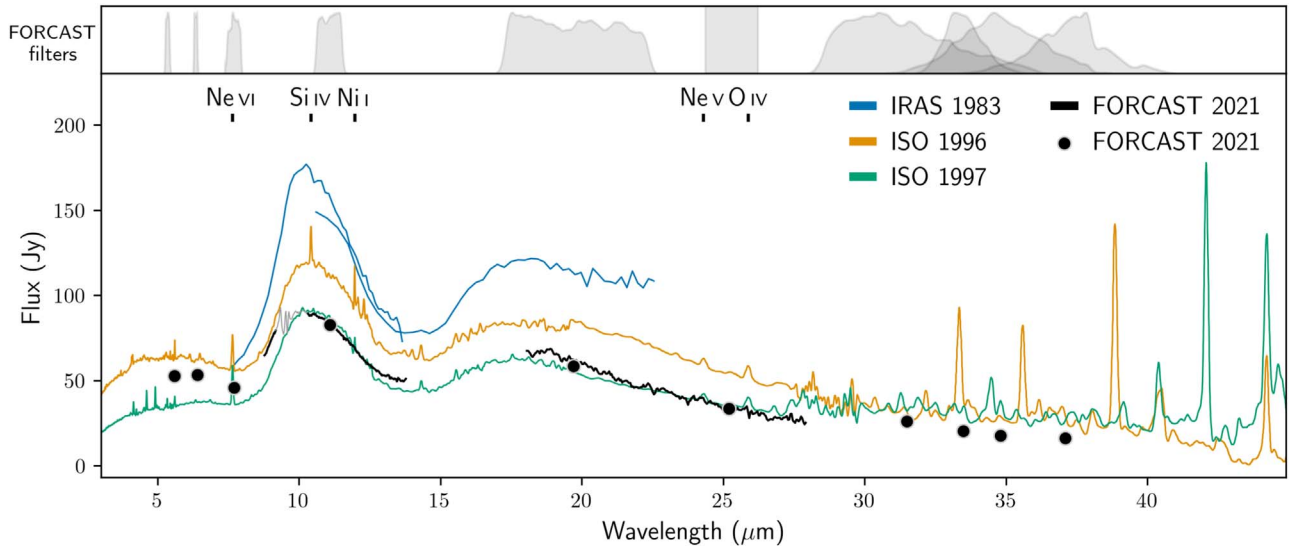

Figure 10. The mid-IR observations of HM Sge. The new FORCAST photometry (red circles) has statistical uncertainties of $\sim$5%. The spectroscopic observations include the region from 9.2–10.3 μm, which is severely affected by atmospheric ozone and is ignored in our analysis. The spectra have been normalized to the flux of the nearest photometric filter. The relative throughput of the FORCAST filters is shown above the data to illustrate the bandwidth.

$10^{-5} M_\odot \, \mathrm{yr}^{-1}$; Höfner & Olofsson 2018). The mechanism needed to drive away this material is thought to be a dust-driven wind. In this scenario pulsations levitate material out to large radii, where it condenses into dust. This dust and any surrounding gas is then driven away radially by radiation pressure. In less hospitable circumstellar environments it is unclear whether harsher radiation restricts the formation of dust and the AGB mass loss mechanism. The slightly fainter far-IR emission may reflect the relaxing of the system, with the colder dust that resulted from the previous outburst leaving the system. The brighter near-IR emission may also signify that the AGB star is returning to producing dust at full capacity, something we see as additional warm dust.

Within the ISO spectra from 1996 and 1997 we see several emission lines in the near-IR and far-IR that are expected to be emanating from HM Sge's surrounding nebula

(Schild et al. 2001). The most prominent is the [Ne VI] $^2P_{3/2}-^2P_{1/2}$ line at 7.6524 μm. This line was observed in 1996/97 with ISO and again in 2005/06 with MIDI (Sacuto et al. 2007). In the MIDI observations, the strongest emission was detected in the best-quality spectra, indicating that the line-emitting region is largely extended. The line was not investigated further due to the limited resolution ($R \sim 200$ around 10.6 μm). It was also not originally observed by IRAS likely due to the low resolution ($R \sim 14$–35) and larger slit width (5′–7.′5) compared to ISO (10–20″). This line is outside the wavelength coverage of our spectroscopic data. The narrow line does, however, fall within our F077 imaging filter, but we do not see a significant increase of the flux in that filter. We also do not see any other clear emission lines in our new FORCAST spectra, indicating that the system is continuing the trend of relaxing after its 1975 outburst.
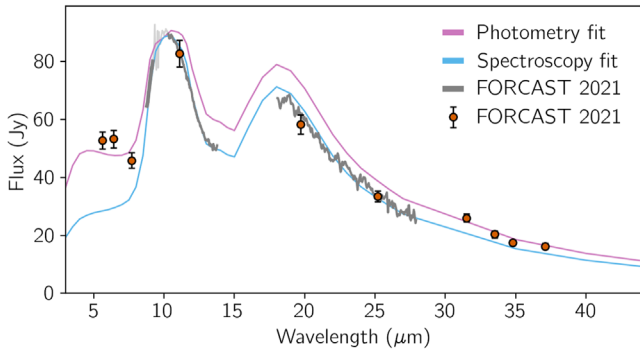
Figure 11. FORCAST photometry and spectra of HM Sge shown with the best-fit radiative transfer models fitted using the DESK; as in Figure 10, the region dominated by atmospheric ozone is shown in gray.

Previous works have attempted to fit the IR data of HM Sge with radiative transfer models to better understand the system's dust. These have included 1D and 2D spherically symmetric model geometries with single and multiple dust-shell components. These works have found different results, fitting the ISO data with better fits for single-shell (Bogdanov & Taranova 2001) and double-shell 1D dust models (Schild et al. 2001; Angeloni et al. 2010). Sacuto et al. (2007) argue that a double-shell dust model would be too extended given the spatial scale of the dust emission in the MIDI observations, and instead support the use of a single-shell model. They also find that this dust distribution shows an increasing level of asymmetry from 8 to 13 μm, with a more extended and patchier distribution in the direction perpendicular to our 130° binary axis.

3.4.1. 1D Radiative Transfer Modeling

We have fitted the FORCAST data with grids of 1D radiative transfer models from the DUSTY code (Elitzur & Ivezić 2001) using the Dusty Evolved Star Kit (DESK; Goldman 2020). We fit the photometry and spectra using the "Silicate-Mix" grids, which include mixtures of different silicate-rich dust species over a range of effective temperatures, inner dust temperatures, and optical depths; the best-fitted models are shown in Figure 11. Fitting separately the photometry and spectroscopy results in best-fit models with a luminosity of $L = 1500$–$2000\ L_\odot$, lower than the previous estimates based on period–luminosity relations and a distance around two to four times our assumed value (5000–10,000 $L_\odot$, Bogdanov & Taranova 2001; Schild et al. 2001). We estimate a gas mass loss rate around $\dot{M} = 4 \times 10^{-6}\ M_\odot\ \mathrm{yr}^{-1}$, similar to values previously derived using DUSTY modeling when accounting for the different assumptions for the distance (Bogdanov & Taranova 2001).[9] These mass loss rates, however, should be used with caution because incorrect model geometry can have a considerable impact on the derived mass loss rates (Wiegert et al. 2020). Additionally, the system's outburst(s) may result in more-significant episodic mass loss. Regardless, the cool component appears to have swiftly returned to producing significant dust post-outburst.

4. Conclusion

We have compared new and archival observations in the IR, optical, and UV to understand how the symbiotic Mira HM Sge has evolved on different scales after its 1975 nova-like outburst.

Changes in UV emission lines and narrowband imaging suggest the environment around HM Sge is evolving. The system has shown a significant decrease in the strength of most of the emission lines detected in 1989. This may either be due to gas being ionized to a higher state or be related to a weaker photoionizing flux from an increase in the separation of the two stellar components due to orbital motion. The morphology of the nebular emission closer to the stellar components shows some changes that may be related to rotation or different parts of the nebula changing in brightness.

New and archival observations do not point to any clear changes linked to the AGB outflow or the most recent outburst. We see some movement of nebular features in new and archival UV narrowband images from 1996 to 2021, corresponding to average outflow velocities of 38 and 78 km s^{-1}. We also detect water emission lines in a symbiotic system for the first time, most of which show velocity shifts of a few km s^{-1} from the systemic velocity. Three new water emission lines are detected with velocity shifts of 31 km s^{-1}, which is consistent with the value (30 km s^{-1}) previously modeled for the outer rim velocity of the accretion disk of the WD.

HM Sge's stellar components have also shown considerable changes over the past few decades. The [Ne V] λ1575/[Ne IV] λ1601 flux ratio in the UV suggests that the effective temperature of the WD is now at least 250,000 K, compared to less than 200,000 K in 1989. We observe a dimming in the I band over the past year, which may be linked to the orbital motion of the system. Infrared photometry and grism spectroscopy targeting the AGB star show a slightly higher near-IR flux and fainter far-IR flux. This may also be related to the orbital motion or may suggest that the system has returned to producing dust at full capacity. By fitting the IR spectral energy distribution (SED) with radiative transfer models we measure an AGB luminosity of $L = 1500$–$2000\ L_\odot$ and a gas mass loss rate of $\dot{M} = 4 \times 10^{-6}\ M_\odot\ \mathrm{yr}^{-1}$. The fairly consistent shape of the AGB SED since the outburst suggests that the AGB star swiftly returned to significant stable dust production.

---

[9] Mass loss rates derived from DUSTY models scale with the luminosity as $\dot{M} \propto r_{\mathrm{gd}}^{1/2} L^{3/4}$, where r_{gd} is the gas-to-dust ratio (Elitzur & Ivezić 2001). As the luminosity scales with distance, and assumed distances have differed in previous works, this is expected to affect the comparison of mass loss rates.

Harris et al. 2020), IPython (Perez & Granger 2007), pandas (pandas development team 2022), Astroalign (Beroiz et al. 2020), Photutils (Bradley et al. 2020).

Appendix
HM Sge Observations

In Table 2 we list the details of our FORCAST imaging observations. In Tables 3 and 4 we show the results of our COS (UV) and EXES (IR) spectroscopic analyses, respectively. In Table 5 we have compiled a list of other spectroscopic and imaging observations relevant to this study including the telescope, filter, wavelength range, and exposure time.

Table 5
Relevant Observations of HM Sge

#	Date	Telescope	Instrument	Type	Filter	Wavelength Range	Exposure Time (s)	Reference	Notes
UV									
1	1978 Jun 6–1983 Oct 15	IUE	SWP, LWR	Spec.		1100–3300 Å		(1)	
2	1992 Dec 1	HST	FOC	Imag.	F190M	1980 Å	596	(2)	
			FOC	Imag.	F253M	2550 Å	596		
			FOC	Imag.	F195W	2090 Å			
3	2021 Mar 21	HST	COS	Spec.	G140L	1230–2050 Å	400[a]	(3)	
			COS	Spec.	G230L	1700–3200 Å	200[a]		
Optical									
4	1983 Sept 15	2.2 m Calar Alto	Coudé	Spec.	[N II], [O III]	6583, 4959 Å	300–900	(4)	
5	1996 Jun 4	NOT	BroCam2	Imag./ Spec.	[N II]	6589 Å	90, 300, 900 × 2	(5)	
			BroCam2	Imag.	Hα cont.	6507 Å	300		
6	1997 Jul 16	NOT	ALFOSC	Imag.	[O II]	3725 Å	120, 2400 × 2		
			ALFOSC	Imag.	[O III]	5012 Å	60, 300		
			ALFOSC	Imag.	[O I]	6311 Å	60		
7	1998 Jun 29–1998 Jul 1	WHT	ISIS	Spec.[b]	R158R	6400–9400 Å		(6)	
			ISIS	Spec.[b]	R600R	6450–7250 Å			
			ISIS	Spec.[b]	R300B	3300–6300 Å			
8	1999 Oct 22	HST	WFPC2	Imag.	F218W	2202 Å	40, 100	(7)	(UV)
			WFPC2	Imag.	F437W	4370 Å	800		
			WFPC2	Imag.	F469W	4694 Å	100		
			WFPC2	Imag.	F487W	4865 Å	200		
			WFPC2	Imag.	F502W	5012 Å	100		[O III]
			WFPC2	Imag.	F547W	5472 Å	2, 20		
			WFPC2	Imag.	F656N	6563 Å	100		Hα
9	2021 Apr 1	HST	WFC3	Imag.	F502N	5009 Å	80 × 2	(3)	[O III]
			WFC3	Imag.	F656N	6561 Å	68 × 2		Hα
			WFC3	Imag.	F658N	6538 Å	60, 3844 × 3		[N II]
IR									
10	1983	IRAS	LRS	Spec.		8–23 μm		(8)	
11	1996 Oct 1	ISO	SWS	Spec.		2.4–45.2 μm	1140	(9)	
			LWS	Spec.		43.1–195.7 μm	822 × 2		
12	1997 May 16	ISO	SWS	Spec.		2.4–45.2 μm	1912	(9)	
13	2005 Jul 23–2006 Jun 11	VLTI	MIDI	Spec.	*N* band	5–13 μm		(10)	
14	2021 Jul 1	SOFIA	FORCAST	Spec.	FOR_G111	8.4–13.7 μm	335	(3)	
	2021 Jul 8		FORCAST	Spec.	FOR_G227	17.6–27.7 μm	121		
15		SOFIA	FORCAST	Imag.	All 10 filters	5.5–38.7 μm	29–220	(3)	(Table 2)

Table 5
(Continued)

#	Date	Telescope	Instrument	Type	Filter	Wavelength Range	Exposure Time (s)	Reference	Notes
16	2021 Jul 1–2021 Jul 8								
	2021 Dec 4	SOFIA	EXES	Spec.	8th order	6.70–6.75 μm	1536	(3)	(Table 4)
	2022 Mar 1	SOFIA	EXES	Spec.	10th order	5.70–5.74 μm	1216		
	2022 Mar 5	SOFIA	EXES	Spec.	7th order	7.56–7.63 μm	2048		
	2022 Apr 27	SOFIA	EXES	Spec.	8th order	6.70–6.76 μm	1024		
	2022 Apr 27	SOFIA	EXES	Spec.	10th order	5.70–5.74 μm	320		
Radio									
17	1992–1997	VLA, MERLIN				0.4, 1.6, 4.9, 22.5 GHz		(11)	
18	1999 Sep 26	VLA				8.56, 23 GHz		(7)	
19	2009 Dec 5	KVN Yonsei				43.1, 42.8, 22.2 GHz		(12)	
Monitoring[c]									
20	1978–1987	SAAO		Imag.	*JHKL*			(13)	
21	1978–1993	Dalmeri		Imag.	*UBVRJHKLMN*			(14)	
22	1978–1999	SAI		Imag.	*JHKLM*			(15)	

Notes.
[a] Observations included three pointings; exposure times listed are for an individual pointing.
[b] Spectropolarimetry.
[c] Data supplemented by the AAVSO.

References. (1) Mueller & Nussbaumer (1985), (2) Hack & Paresce (1993), (3) this work, (4) Solf (1984), (5) Corradi et al. (1999), (6) Schmid et al. (2000), (7) Eyres et al. (2001), (8) Neugebauer et al. (1984), (9) Schild et al. (2001), (10) Sacuto et al. (2007), (11) Richards et al. (1999), (12) Cho & Kim (2010), (13) Munari & Whitelock (1989), (14) Yudin et al. (1994), (15) Taranova & Shenavrin (2000).

ORCID iDs

Steven R. Goldman ⓘ https://orcid.org/0000-0002-8937-3844
Ravi Sankrit ⓘ https://orcid.org/0000-0001-8858-1943
Edward Montiel ⓘ https://orcid.org/0000-0003-2553-4474
Sean Garner ⓘ https://orcid.org/0000-0002-2748-9809
Nathan Wolthuis ⓘ https://orcid.org/0000-0001-5201-3223
Nicole Karnath ⓘ https://orcid.org/0000-0003-3682-854X

References

Andriantsaralaza, M., Ramstedt, S., Vlemmings, W. H. T., & De Beck, E. 2022, A&A, 667, A74
Angeloni, R., Contini, M., Ciroi, S., & Rafanelli, P. 2010, MNRAS, 402, 2075
Astropy Collaboration, Price-Whelan, A. M., Sipőcz, B. M., et al. 2018, AJ, 156, 123
Astropy Collaboration, Robitaille, T. P., Tollerud, E. J., et al. 2013, A&A, 558, A33
Belczyński, K., Mikołajewska, J., Munari, U., Ivison, R. J., & Friedjung, M. 2000, A&AS, 146, 407
Beliakina, T. S., Gershberg, R. E., & Shakovskaia, N. I. 1978, SvAL, 4, 219
Belyakina, T. S., Gershberg, R. E., & Schakhovskaya, N. I. 1979, SvAL, 5, 349
Beroiz, M., Cabral, J., & Sanchez, B. 2020, A&C, 32, 100384
Bogdanov, M. B., & Taranova, O. G. 2001, ARep, 45, 44
Bradley, L., Sipőcz, B., Robitaille, T., et al. 2020, astropy/photutils: v1.0.0, Zenodo, doi:10.5281/zenodo.4044744
Bregman, J. D. 1982, BAAS, 14, 982
Cho, S.-H., & Kim, J. 2010, ApJ, 719, 126
Ciatti, F., Mammano, A., & Vittone, A. 1979, A&A, 79, 247
Corradi, R. L. M., Ferrer, O. E., Schwarz, H. E., Brand i, E., & García, L. 1999, A&A, 348, 978
Dokuchaeva, O. D. 1976, IBVS, 1189, 1
Elitzur, M., & Ivezić, Ž. 2001, MNRAS, 327, 403
Engels, D., & Bunzel, F. 2015, A&A, 582, A68
Eyres, S. P. S., Bode, M. F., Taylor, A. R., Crocker, M. M., & Davis, R. J. 2001, ApJ, 551, 512

Fonfría, J. P., Cernicharo, J., Richter, M. J., & Lacy, J. H. 2008, ApJ, 673, 445
Formiggini, L., Contini, M., & Leibowitz, E. M. 1995, MNRAS, 277, 1071
Gaia Collaboration, Brown, A. G. A., Vallenari, A., et al. 2018, A&A, 616, A1
Girard, T., & Willson, L. A. 1987, A&A, 183, 247
Goldman, S. R. 2020, JOSS, 5, 2554
Goldman, S. R., Sankrit, R., Wolthuis, N., et al. 2022, RNAAS, 6, 159
Goldman, S. R., van Loon, J. T., Zijlstra, A. A., et al. 2017, MNRAS, 465, 403
Gray, M. D., Etoka, S., Richards, A. M. S., & Pimpanuwat, B. 2022, MNRAS, 513, 1354
Guerrero, M. A., Suzett Rechy-García, J., & Ortiz, R. 2020, ApJ, 890, 50
Hack, W. J., & Paresce, F. 1993, PASP, 105, 1273
Harris, C. R., Millman, K. J., van der Walt, S. J., et al. 2020, Natur, 585, 357
Herter, T. L., Adams, J. D., Gull, G. E., et al. 2018, JAI, 7, 1840005
Hinkle, K. H., Fekel, F. C., Joyce, R. R., & Wood, P. 2013, ApJ, 770, 28
Höfner, S., & Olofsson, H. 2018, A&ARv, 26, 1
Hunter, J. D. 2007, CSE, 9, 90
Indriolo, N., Neufeld, D. A., Barr, A. G., et al. 2020, ApJ, 894, 107
Kenyon, S. J. 1986, The Symbiotic Stars (Cambridge: Cambridge Univ. Press), 295
Kwok, S., Bignell, R. C., & Purton, C. R. 1984, ApJ, 279, 188
Kwok, S., & Leahy, D. A. 1984, ApJ, 283, 675
Lee, H.-W., & Kang, S. 2007, ApJ, 669, 1156
Liimets, T., Corradi, R. L. M., Jones, D., et al. 2018, A&A, 612, A118
Merc, J., Gális, R., & Wolf, M. 2019, RNAAS, 3, 28
Merrill, P. W. 1940, Spectra of Long-period Variable Stars (Chicago, IL: Univ. Chicago Press)
Mueller, B. E. A., & Nussbaumer, H. 1985, A&A, 145, 144
Muerset, U., Wolff, B., & Jordan, S. 1997, A&A, 319, 201
Munari, U., & Whitelock, P. A. 1989, MNRAS, 237, 45P
Murset, U., & Nussbaumer, H. 1994, A&A, 282, 586
Mürset, U., & Schmid, H. M. 1999, A&AS, 137, 473
Neugebauer, G., Habing, H. J., van Duinen, R., et al. 1984, ApJL, 278, L1
Nussbaumer, H., & Vogel, M. 1990, A&A, 236, 117
Olofsson, H., Khouri, T., Sargent, B. A., et al. 2022, A&A, 665, A82
Palen, S., Balick, B., Hajian, A. R., et al. 2002, AJ, 123, 2666
pandas development team, T 2022, pandas-dev/pandas: Pandas v1.4.3, Zenodo, doi:10.5281/zenodo.6702671

Perez, F., & Granger, B. E. 2007, CSE, 9, 21
Reed, D. S., Balick, B., Hajian, A. R., et al. 1999, AJ, 118, 2430
Richards, A. M. S., Bode, M. F., Eyres, S. P. S., et al. 1999, MNRAS, 305, 380
Richter, M. J., Dewitt, C. N., McKelvey, M., et al. 2018, JAI, 7, 1840013
Sacuto, S., Chesneau, O., Vannier, M., & Cruzalèbes, P. 2007, A&A, 465, 469
Sahai, R., Huang, P. S., Scibelli, S., et al. 2022, ApJ, 929, 59
Schild, H., Eyres, S. P. S., Salama, A., & Evans, A. 2001, A&A, 378, 146
Schmid, H. M., Corradi, R., Krautter, J., & Schild, H. 2000, A&A, 355, 261
Solf, J. 1983, ApJL, 266, L113
Solf, J. 1984, A&A, 139, 296
Stauffer, J. R. 1984, ApJ, 280, 695
Taranova, O. G., & Shenavrin, V. I. 2000, AstL, 26, 600
Temi, P., Hoffman, D., Ennico, K., & Le, J. 2018, JAI, 7, 1840011

Toalá, J. A., Botello, M. K., & Sabin, L. 2023, ApJ, 948, 14
Tomov, N. A., Tomova, M. T., & Bisikalo, D. V. 2007, MNRAS, 376, L16
Tomov, T., Zamanov, R., Gałan, C., & Pietrukowicz, P. 2017, AcA, 67, 225
van der Walt, S., Colbert, S. C., & Varoquaux, G. 2011, CSE, 13, 22
Virtanen, P., Gommers, R., Oliphant, T. E., et al. 2020, NatMe, 17, 261
Wallerstein, G. 1978, PASP, 90, 36
Wannier, P. G., Sahai, R., Andersson, B. G., & Johnson, H. R. 1990, ApJ, 358, 251
Webster, B. L., & Allen, D. A. 1975, MNRAS, 171, 171
Wiegert, J., Groenewegen, M. A. T., Jorissen, A., Decin, L., & Danilovich, T. 2020, A&A, 642, A142
Yudin, B., Munari, U., Taranova, O., & Dalmeri, I. 1994, A&AS, 105, 169